中国光学（中英文） Chinese Optics 核心期刊

Homodyne Littrow grating interferometer for two-degrees-of-freedom measurement

QIAN Xin-ge, LIANG Xu, LIU Zhao-wu, GAO Xu, JIN Si-yu, ZHANG Yao-yu, LI Wen-hao

Citation:
QIAN Xin-ge, LIANG Xu, LIU Zhao-wu, GAO Xu, JIN Si-yu, ZHANG Yao-yu, LI Wen-hao. Homodyne Littrow grating interferometer for two-degrees-of-freedom measurement[J]. *Chinese Optics*, 2026, 19(3): 689-700. doi: 10.37188/CO.EN-2025-0019
潜辛格, 梁旭, 刘兆武, 高旭, 金思宇, 张尧禹, 李文昊. 零差利特罗光栅双轴干涉仪[J]. 中国光学, 2026, 19(3): 689-700. doi: 10.37188/CO.EN-2025-0019

View online: https://doi.org/10.37188/CO.EN-2025-0019

Articles you may be interested in

Omnidirectional spatial monocular vision indoor localization measurement based on a two-degree-of-freedom rotary platform
基于双自由度转台的全向空间单目视觉室内定位测量方法
Chinese Optics. 2024, 17(3): 605 https://doi.org/10.37188/CO.2023-0106

Simultaneous measurement of radial angular displacement and longitudinal linear displacement with cascade metasurfaces
利用级联超构表面同时测量径向角位移和纵向线位移
Chinese Optics. 2025, 18(5): 1016 https://doi.org/10.37188/CO.2025-0033

The measurement method of heliostat surface shape error based on photogrammetry
基于摄影测量的定日镜面形误差检测方法研究
Chinese Optics. 2023, 16(2): 425 https://doi.org/10.37188/CO.2021-0210

Error modeling and analysis of dual-frequency laser interferometry in scanning beam interference lithography system
扫描干涉曝光系统中双频激光干涉测量误差建模与分析
Chinese Optics. 2025, 18(2): 224 https://doi.org/10.37188/CO.2024-0149

Three-dimensional surface shape reconstruction of fiber bragg gratings in a ring arrangement
环形布设光纤布拉格光栅的三维曲面形状重构
Chinese Optics. 2024, 17(2): 398 https://doi.org/10.37188/CO.2023-0088

A non-null interferometry for concave aspheric surface
凹非球面的非零位干涉检测技术
Chinese Optics. 2024, 17(1): 140 https://doi.org/10.37188/CO.2023-0042

文章编号 2097-1842(2026)03-0689-12

Homodyne Littrow grating interferometer for two-degrees-of-freedom measurement

QIAN Xin-ge[1,2], LIANG Xu[1 *], LIU Zhao-wu[1], GAO Xu[3], JIN Si-yu[1], ZHANG Yao-yu[1], LI Wen-hao[1]

（1. *Changchun Institute of Optics*, *Fine Mechanics and Physics*, *Chinese Academy of Sciences*, *Changchun* 130033, *China*;

2. *University of Chinese Academy of Sciences*, *Beijing* 100049, *China*;

3. *College of Optoelectronic Engineering*, *Changchun University of Science and Technology*, *Changchun* 130022, *China*）

* *Corresponding author*, *E-mail*: *liangxu@ciomp.ac.cn*

Abstract: In response to the current demand for high-precision planar displacement measurements in advanced manufacturing equipment, this paper proposes an *xz* dual-axis grating interferometer. The system adopts a biaxial Littrow incident light path structure, established using a biaxial beam splitter mirror and right-angled prism mirror. The relationship between the parallelism of the outgoing beam, the beam spacing, and the position and angle of the incident light is analyzed. Experimental results verify the feasibility and measurement performance of the proposed interferometer. The grating interferometer achieves a displacement resolution of 4 nm along the *x*-axis and 7 nm along the *z*-axis. After correction using the Heydemann algorithm, the periodic nonlinear error is reduced to ±5 nm. Over a travel range of 10 mm, the measurement accuracies are ±30 nm along the *x*-axis and ±100 nm along the *z*-axis, respectively. Finally, the influence of the surface error introduced by the non-coincident incident structure on the measurement results is discussed.

Key words: grating interferometer; two-degree-of-freedom displacement measurement; Littrow structure; surface shape error

收稿日期:2025-03-06; **修订日期**:2025-04-07

基金项目:国家自然科学基金青年项目（No. 52305592）; 吉林省科技发展计划（No. 20240404065ZP; No. YDZJ202401295ZYTS）; 吉林省科技厅自然科学基金面上项目（No. 20230101217JC）

Supported by National Natural Science Foundation of China (No. 52305592); Jilin Provincial Scientific and Technological Development Program (No. 20240404065ZP; No. YDZJ202401295ZYTS); Natural Science Foundation of Jilin Province (No. 20230101217JC)

零差利特罗光栅双轴干涉仪

潜辛格[1,2], 梁　旭[1*], 刘兆武[1], 高　旭[3], 金思宇[1], 张尧禹[1], 李文昊[1]
（1. 中国科学院长春光学精密机械与物理研究所, 吉林 长春 130033；
2. 中国科学院大学, 北京 100049；
3. 长春理工大学 光电工程学院, 吉林 长春 130022）

摘要: 针对目前先进制造设备对于高精度平面位移测量的需求, 本文提出了一种 *xz* 双轴光栅干涉仪, 通过偏置分束镜配合直角棱镜反射镜搭建双侧 Littrow 入射光路结构。分析了出射光束平行性、光束间距与入射光位置、角度之间的关系。实验验证了所提干涉仪的可行性和测量性能, 光栅干涉仪在 *x* 轴和 *z* 轴上分别实现 4 nm、7 nm 的位移分辨率, 经海德曼算法修正后, 将周期非线性误差抑制至±5 nm 以内。10 mm 行程范围内, *x* 轴和 *z* 轴分别获得±30 nm 和±100 nm 的测量精度。最后讨论了由于非共点入射结构所引入的面型误差对测量结果的影响。

关　键　词: 光栅干涉; 二自由度位移测量; 利特罗结构; 面形误差
中图分类号: O439; TH741　　**文献标志码:** A　　**doi:** 10.37188/CO.EN-2025-0019　　**CSTR:** 32171.14.CO.EN-2025-0019

1 Introduction

Advanced manufacturing equipment, such as ultra-precision machine tools and high-end lithography machines, typically involves the worktable primarily executing planar two-freedom movements, with vertical displacement and angular deviations across the remaining three-degrees-of-freedom (three-DOF) existing as accompanying errors[1-3]. Compared with laser interferometry, grating interferometry uses the grating pitch as a reference and has a shorter exposed optical path length, which does not change with the travel distance, offering superior resistance to environmental disturbances[4-10]. In addition, the grating interferometer has a probe head that is aligned vertically along the scale grating and thus a layout that is more flexible and compact, making it easier to integrate into machine[9-13]. As early as 2009, ASML, used a grating interferometer for measurement with six-DOF in their NXT series of lithography machines. In these machines, multiple measurement heads are distributed in the detection space according to needs, with a single measurement head capable of simultaneously measuring two-DOF for displacement in the *xz*/*yz* planes. The six-DOF for the position and posture of the grating are calculated by combining the interferometric measurements for multiple axes[14-17].

In the multi-probe multi-DOF grating interferometer system, the detection performance of each probe fundamentally affects the overall accuracy of the multi-DOF displacement measurement. Early grating interferometers adopted a scheme in which the laser was perpendicularly incident on the scale grating. Gao[18], Hsieh[19], Li[20-22], and other research groups conducted extensive studies on this topic. A notable development in this area is Kimura's subnanometer two-axis surface encoder[23-25], which simultaneously measures displacement in and out of the grating plane. This system has achieved measurement errors of 300 nm along the *x*-axis and 150 nm along the *z*-axis, with resolution of approximately 0.5 nm for both axes. Building on this foundation, a research group from Tsinghua University[26] proposed a heterodyne two-axis grating interferometer system. By incorporating the principle of heterodyne interference to enhance the anti-interference ability of the system, they eliminated the need for a four-step phase-shift system to realize the displacement direction, resulting in a simpler and more compact design. The system achieved measurement ac-

curacy of 6.37 nm and 3.69 nm in the *x*- and *z*-directions, respectively. Moreover, a research group at Guilin University of Electronic Science and Technology used a pyramid prism to diffract light twice within a similar structure[27-28], thus improving the optical subdivision factor and increasing the resolution of the system. They also analyzed and compensated for the nonlinear error in the system, reducing the peak value of the nonlinear error from 17 nm to 7 nm.

It has been found that in vertically incident grating interferometers, when the scale grating moves in the *z*-direction, the reference and measurement spots readily separate, resulting in a contrast reduction of the interference signal and a small measurement range of out-of-plane displacement[29]. To solve these problems, scholars have proposed the Littrow configuration, which is characterized by self-collimation of the grating at a right angle to the incident light, causing the first-order diffracted light of the grating to coincide with the incident light. This improves the off-axis tolerance of the grating and provides new possibilities for large-range out-of-plane measurements[30-32]. De Groot earlier proposed a high-performance homodyne two-DOF grating interferometer[33], which uses multiple gratings—all in the Littrow configuration—for *x*/*z* two-DOF displacement measurement. Utilizing the zeroth- and second-order diffracted light for synchronous displacement measurements, the measurement error introduced by the grating calibration is reduced. Wang's research group proposed an ultra-precision, spatially separated heterodyne Littrow planar grating encoder[34], integrating optical components such as beam splitter and pyramid prism to make the optical path in the read head more compact. This system achieved a theoretical resolution of 50 pm in the *x*-axis and 25 pm in the *z*-axis. Moreover, the corner cube prism used in the system increased the angular tolerance and off-axis tolerance. Lin proposed a three-axis grating interferometer capable of high-resolution and long-range displacement measurements[35–36]. Through double-grating beam splitting, the light source was divided into four beams of parallel light that entered the interferometer. A refraction grating set before the measurement grating folded the light such that it struck the measurement and reference gratings under the Littrow configuration. This system realized a theoretical *z*-axis displacement measurement range of 1 263 mm. However, owing to the low-groove-density of the grating (8 μm), the theoretical resolution was only 4 nm. To improve the utilization of light energy, a four-step relief structure was adopted in the refractive grating design, which increased the overall difficulty of processing.

This paper designed a *xz* two-DOF homodyne grating interferometer based on the Littrow incidence condition. By using a biased beam splitter to obtain parallel dual detection beams, the intensity ratio of the reference and measurement beams can be optimized simply by rotating the light source posture, without compromising the intensity of the detection beams. This allows for a simple and efficient acquisition of the highest quality interference signals. A symmetrical bilateral Littrow optical path structure is constructed using a right-angle reflection prism in combination with a plane mirror. This ensures autocollimation incidence even with gratings of arbitrarily high line densities. While enhancing the angular tolerance of the grating read head, this structure is highly conducive to integration and miniaturization. Finally, a prototype was built in this paper. The displacement measurement performance of the *x*-axis and *z*-axis was tested separately, and the error influence when the detection beams are non-coincident was analyzed.

2 Measurement principles

2.1 Principle of measuring biaxial displacement

Figure 1 is an optical path diagram of the homodyne biaxis grating interferometer. The linearly polarized light emitted by the laser diode is divided

into two parallel beams after passing through the non-polarizing beam splitter (NPBS), which is placed at 45°. After the two parallel beams enter the polarization beam splitter 1(PBS1), the P-polarized component is transmitted as the reference light, and the S-polarized component is reflected as the measurement light. Because the Littrow diffraction angle of the grating positively correlates with the groove density, to adapt to the high-groove-density grating used in this study and avoid the problem of single refraction grazing incidence on the reflector. The Littrow configuration is constructed combining the quadratic refraction mode with a right-angled prism reflector. Here, the diffracted light on the right side, reflected by M2, is designated as the -1st-order diffracted light, and the diffracted light on the left side, reflected by M3, is designated as the +1st-order diffracted light. The ±1st-order diffracted beams return along their original paths and pass through the quarter-wave plate 1(QWP1) twice to become the P-polarized components. The reference light, after being reflected by M1 and returning along its original path, becomes S-polarized after passing through QWP2 twice. The ±1st-order diffracted beams are then combined with the reference light at the polarization beam splitter, resulting in interference. The two interference signals are expressed as:

$$\begin{cases} I_{X+1} = U_{X+1} \cdot \overline{U_{X+1}} = 2U_0^2(1+\cos(\Omega+\phi)) \\ I_{X-1} = U_{X-1} \cdot \overline{U_{X-1}} = 2U_0^2(1+\cos(-\Omega+\phi)) \end{cases}, \tag{1}$$

where I_{X+1} and U_{X+1} are the interference signal intensity and electric field intensity of the +1st-order diffracted light, I_{X-1} and U_{X-1} are the interference signal intensity and electric field intensity of the −1st-order diffracted light. $\Omega = \Delta x \cdot 2\pi/g$ represents the phase change due to the Doppler frequency shift introduced by the grating's displacement along the x-axis, and g is the grating pitch used. $\phi = \Delta z \cdot 2\pi/g\cos\theta$ represents the phase change in the optical path due to the grating's displacement along the z-axis, θ is the diffraction angle under the Littrow configuration.

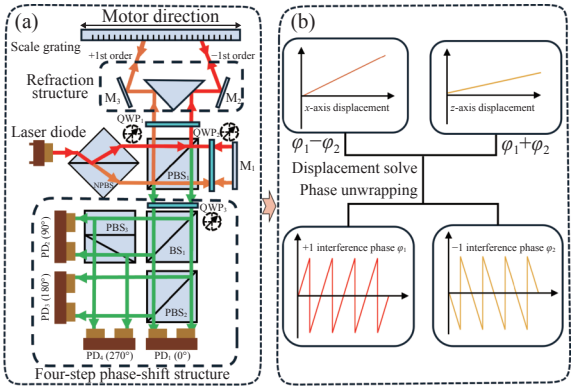

Fig. 1 (a) Optical path diagram of the *xz* homodyne two-DOF grating interferometer. (b) Displacement solve principle

The two interference signals then enter the four-step phase-shift structure comprising BS1, PBS2, and PBS3, after QWP3. The four array detectors receive sinusoidal signals with phase differences of 0°, 90°, 180°, and 270°. After processing, four standard sine and cosine signals are obtained:

$$\begin{cases} S_{X+1} = \dfrac{I_{X+1}(0°) - I_{X+1}(180°)}{I_{X+1}(0°) + I_{X+1}(180°)} = \sin(\Omega+\phi) \\ S'_{X+1} = \dfrac{I_{X+1}(90°) - I_{X+1}(270°)}{I_{X+1}(90°) + I_{X+1}(270°)} = \cos(\Omega+\phi) \\ S_{X-1} = \dfrac{I_{X-1}(0°) - I_{X-1}(180°)}{I_{X-1}(0°) + I_{X-1}(180°)} = \sin(-\Omega+\phi) \\ S'_{X-1} = \dfrac{I_{X-1}(0°) - I_{X-1}(180°)}{I_{X-1}(0°) + I_{X-1}(180°)} = \cos(-\Omega+\phi) \end{cases}. \tag{2}$$

The corresponding interference phase is obtained by applying the arctangent function and phase unwrapping to the two interference signals. The displacement in the x- and z-directions is expressed as:

$$\Delta x = \frac{g}{4\pi} \cdot \left(\arctan\left(\frac{S_{X+1}}{S'_{X+1}}\right) - \arctan\left(\frac{S_{X-1}}{S'_{X-1}}\right) \right) = \frac{g}{2\pi} \cdot \Omega$$

$$\Delta z = \frac{g}{4\pi \cdot \cot\theta} \left(\arctan\left(\frac{S_{X+1}}{S'_{X+1}}\right) + \arctan\left(\frac{S_{X-1}}{S'_{X-1}}\right) \right) = \frac{g}{2\pi \cdot \cot\theta} \cdot \phi \quad . \tag{3}$$

2.2 Generation of parallel light beams

The interferometer optical path structure proposed in this paper enables the simple and direct generation of dual parallel probe beams through the laser diode and NPBS. However, the position where the beam is incident on the NPBS, as well as the refractive index, size, and bias angle of the NPBS

itself, affect the parallelism and beam spacing of the dual parallel beams. An analysis of the aforementioned factors is presented here. As shown in Fig. 2(a) (color online), we let the length of the right-angled side of the NPBS be l. When the horizontal probe laser is incident on the NPBS at an angle θ_1, the corresponding refracted angle is $\theta_2 = \arcsin(n_1/(n_2 \cdot \sin\theta_1))$, and the angle of the emerging beam θ_3 is expressed as:

$$\theta_3 = \arcsin\left(\frac{n_2}{n_1}\sin\left(\arcsin\left(\frac{n_2}{n_1}\sin\theta_1\right)\right)\right) = \theta_1 \quad , \quad (4)$$

where n_1 and n_2 are the refractive indices of air and the NPBS, respectively, and the angle θ_4 between the light emerging from the upper end and the horizontal axis is expressed as:

$$\theta_4 = \frac{\pi}{2} - \theta_1 - \theta_3 = \frac{\pi}{2} - 2\theta_1 \quad . \quad (5)$$

It is seen from the above formula that when the incidence angle is 45°, the angle between the outgoing light and horizontal plane is 0°. For the lower end of the outgoing light beam, it is as if the light passes through a parallel plate of glass, and the outgoing light beam thus remains parallel to the incident light beam.

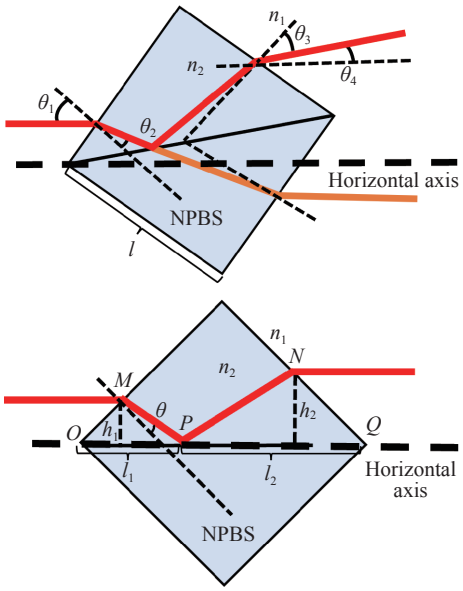

Fig. 2 (a) Relation between the NPBS bias angle and the exiting light deflection angle. (b) Relation between incident height, NPBS refractive index and exit height

Next the spacing between the two output beams is considered. As shown in Figure 2(b) (color online), the θ_1 is set to 45°. The vertical distances from the incident light and the emerging light at the upper end to the beam splitter surface are denoted h_1 and h_2, respectively. Using Snell's law and the sine theorem, the distance l_1 from the vertex O of the beam splitter to the detection point P is expressed as:

$$l_1 = \frac{\sqrt{2}h_1 \sin\left(\frac{\pi}{2} + \theta_2\right)}{\sin\left(\frac{\pi}{4} - \theta_2\right)} \quad . \quad (6)$$

As triangles OMP and ONQ are similar, the height h_2 of the final emerging beam is expressed as:

$$h_2 = l \cdot \frac{\sin\left(\frac{\pi}{4} - \arcsin\left(\frac{\sqrt{2}n_1}{2n_2}\right)\right)}{\sin\left(\frac{\pi}{2} + \arcsin\left(\frac{\sqrt{2}n_1}{2n_2}\right)\right)} - h_1 \quad . \quad (7)$$

The NPBS used in this system has a size of 15 mm and is made from H-K9L optical glass, with a refractive index of approximately 1.52. Considering the compactness of the subsequent optical path and the size of the photosensitive area of the array photodiode, the height of the incident beam h_1 is set at 1.5 mm, the corresponding outgoing beam height h_1 is approximately 3.5 mm, and the spot spacing of the double-parallel beam is approximately 7 mm.

As the reference optical path uses a plane mirror for reflection and the measurement optical path uses the diffracted light from the grating, if the light intensity on the measurement path is the same as that on the reference path after PBS1, the light intensity on the reference path is much greater than that on the measurement path on the final receiving surface owing to the diffraction efficiency of the grating, which reduces the contrast of the interference signal. To improve signal contrast, the light source is rotated to change its polarization state, thereby altering the light splitting ratio after PBS1. This ensures that the light intensities on the reference and measurement paths are as consistent as

possible when the beams recombine at PBS1. The holographic grating used in this experiment has a diffraction efficiency of approximately 15% for ±1st-order diffraction under the Littrow configuration. Experimental tests have shown that when the light source polarization angle is approximately 72°, the light intensity is equal in the two arms, and the fringe contrast is optimal.

3 Performance tests

3.1 Experimental equipment

To verify the displacement measurement performance of the proposed grating interferometer, the precision comparison system shown in Fig. 3(a) is set up. The system comprises two parts: the grating interferometer and laser interferometer. In the grating interferometer, the light source is linearly polarized with a wavelength of 670 nm (CPS-670F, Thorlabs). A high-precision linear stage (XML-210s, Newport) moves the scale grating, and the interference signals generated by the grating interferometer are detected and collected by a photoelectric detector (S5981/-10, Hamamatsu) in conjunction with a data acquisition card (PCI-6229, NI). A laser interferometer (with a 5517-D light source and 10706B interferometer components, Keysight) is placed alongside the displacement stage for comparison with true displacement values. To reduce the effects of Abbe error on the measurements, the position of the laser interferometer is adjusted so that the measurement axis of the laser interferometer is essentially collinear with the surface of the measurement grating. The experimental environmental temperature and humidity are measured using an environmental detector (TSP01, Thorlabs), and the refractive index of air is corrected using an empirical formula for wavelength adjustments.

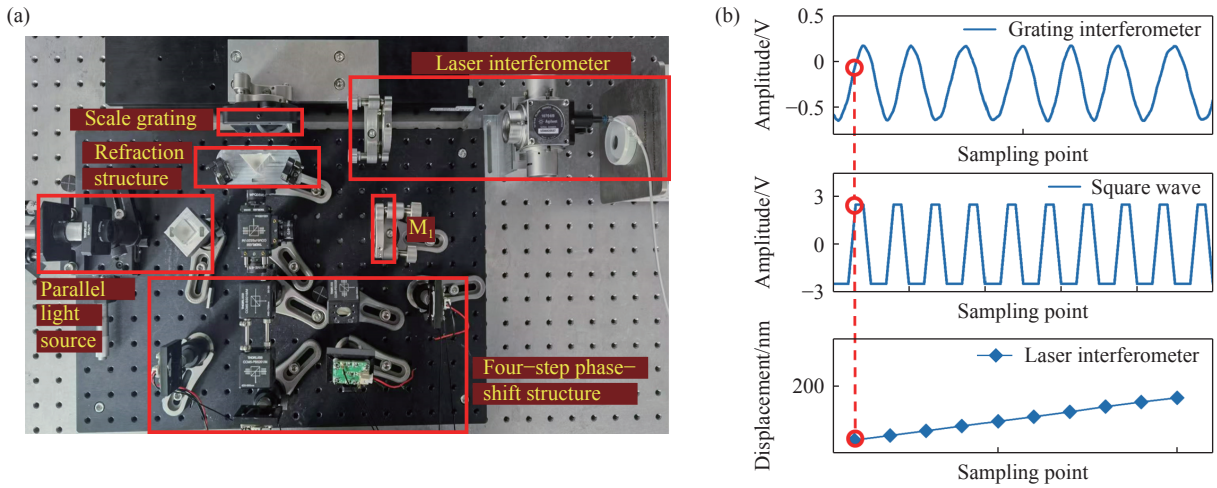

Fig. 3 (a) Photograph of the setup. (b) Synchronous trigger schematic

To ensure synchronous data collection by the two data acquisition cards, as shown in Fig. 3(b), the square wave signal from the PCI-6229 itself is used as the sampling clock. When the rising edge of the reference square wave is detected, both the N1230A and PCI-6229 are triggered to collect data from the laser interferometer and grating interferometer simultaneously, ensuring good temporal synchronization between the data collected by the two data acquisition cards.

3.2 Experimental tests

3.2.1 Displacement measurement and accuracy test

We first verify the measurement accuracy of the proposed system under short range conditions by running the displacement table through a distance of 500 μm at a speed of 10 μm/s. The measurements are shown in Fig. 4(a) (color online). These results contain a linear error of approximately 200 nm, which is primarily due to the cosine

error introduced by the grating installation and the calibration error in the grating's groove density. This linear error is an inherent system error, which can be directly compensated for and removed through calibration. This is not discussed in detail here.

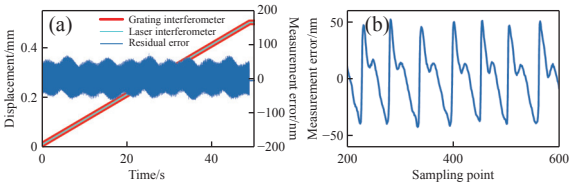

Fig. 4　(a) 500 μm motion and residual error. (b) Partial magnification of residual error

After correcting the liner error, the residual error is shown by the blue line in Fig. 4(a). The overall error band is approximately ±50 nm. Upon zooming in, as shown in Fig. 4(b) (color online), the error has obvious periodicity, which is attributed to direct current (DC) bias, amplitude deviation, and phase error between the two interference signals. By applying the Heydemann correction algorithm to the non-orthogonal interference signal, the specific values of DC, amplitude, and phase errors are obtained, and the fitted values are then used to correct the original signal in real time and thus obtain a more accurate orthogonal signal. Figure 5(a) (color online) shows the Lissajous circles of the signal before and after correction, whereas Fig. 5(b) (color online) shows the residual error before and after correction. The error band is reduced from the original ±50 nm to ±5 nm, demonstrating the effectiveness of the compensation.

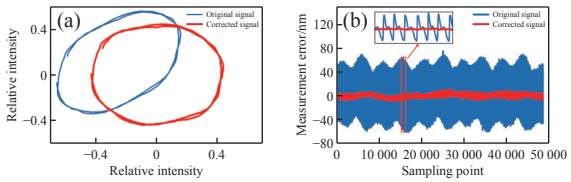

Fig. 5　(a) Lissajou figure before and after correction. (b) Comparison of residual error before and after correction

3.2.2　Resolution test

Next the displacement resolution of the system is tested. The grating interferometer used in this study has an optical subdivision. Combined with the 16-bit data acquisition card, when the effective subdivision multiple is 4 096, giving theoretical resolutions of 68 pm for the *x*-axis and 82 pm for the *z*-axis. However, because of the environmental disturbance and electronic noise and other factors, the displacement measurements of the grating interferometer can not reach the theoretical resolution. Therefore, a step test is conducted to assess the resolution. Figure 6 (color online) shows the results of the step tests on the *xz* dual axes. Figures 6(a) and 6(c) are the original signals of the step tests on the *x*-axis and *z*-axis, respectively. Figures 6(b) and 6(d) are the results of the step tests on the *x*-axis and *z*-axis, respectively. By zooming in on parts of Figures 6(a) and 6(c), it can be seen that the amplitude of the electronic noise in the *x*-axis direction is approximately 0.019 V, and the amplitude of the electronic noise in the *z*-axis direction is approximately 0.025 V. The experiments show that the proposed grating interferometer can resolve step displacements of 4 nm along the *x*-axis and 7 nm along the *z*-axis.

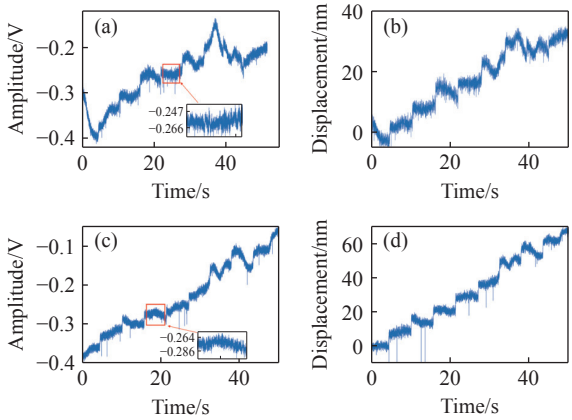

Fig. 6　(a) The original signal of the *x*-axis step test. (b) Results of the step test along the *x*-axes. (c) The original signal of the *z*-axis step test. (d) Results of the step test along the *z*-axes

3.2.3　Repeatability analysis and stability test

To measure the repeatability accuracy of the grating interferometer, the displacement table is moved back and forth 10 times along the *x*-axis

between the origin and the 500 μm position. Fig. 7 (color online) shows the box-plot and the normal distribution curves of the grating interferometer and laser interferometer. In the box-plot, the horizontal lines of the box plot represent the average of the 10 measurements of the laser interferometer and grating interferometer. The length of the box plot represents the standard deviation (1σ) of the measurements. The whisker lines above and below the box indicate the maximum and minimum measurements. The results show that the repeatability of the grating interferometer is better than 40 nm on *x*-axis, with the distribution of multiple measurements closely matching that of the laser interferometer.

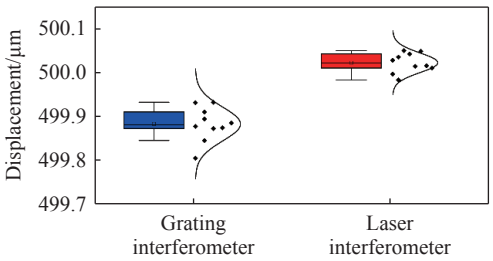

Fig. 7 Repeatability test results

3.2.4 Long range measurement experiment

After determining the short-distance measurement accuracy, resolution data, and repeatability accuracy of the grating interferometer, the displacement measurement accuracy over a long range is assessed, demonstrating the advantages of the interferometer system designed in this paper in the *z*-direction measurement range. The grating is moved 10 mm along the *x*- and *z*-axis at a speed of 0.2 mm/s, respectively. After the linear error in the measurement results is revised and the periodic nonlinear error is corrected by the Heydemann correction algorithm, the measurements along the *x*- and *z*-axes as shown in Figures 8(a) and 8(b) (color online). Taking a sliding average (with a window width of 200 data points), the error of the two measurement axes is controlled at approximately ±30 nm for the *x*-axis and ±100 nm for the *z*-axis, respectively.

Similarly, we conducted multiple 10 mm displacement tests on the *x*-axis and *z*-axis to verify their repeatability. The results are shown in Figure 9 (color online). In the *x*-axis test results, the distribution of results from the grating interferometer is close to that of the commercial laser interferometer. In the *z*-axis test results, the distribution of results from the grating interferometer is slightly worse than that of the commercial laser interferometer, but overall, they are still relatively close.

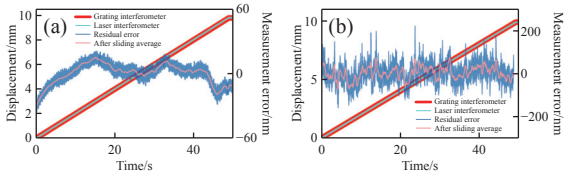

Fig. 8 (a) Measurement for displacement of 10 mm along the *x*-axis. (b) Measurement for displacement of 10 mm along the *z*-axis

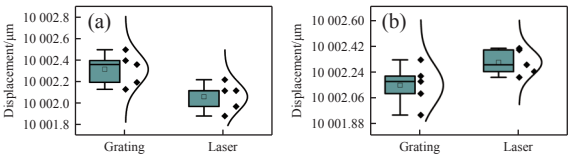

Fig. 9 (a) The results of the 10 mm displacement repeatability test on the *x*-axis. (b) The results of the 10 mm displacement repeatability test on the *z*-axis

Considering that the two beams of the measurement path in the experiment are incident on different positions of the grating surface, the interference phases of the two diffracted lights corresponding to the measurements are different under the influence of the grating surface shape error, which in turn introduces displacement measurement deviation[37-38]. The surface shape error specifically includes: grating substrate error and grating line error. The relationship between the diffracted light wavefront Δ and the substrate error H and line error W is as follows:

$$\Delta = 2H\cos\theta_m + W\frac{\lambda'}{d} \quad . \tag{8}$$

The diffracted light wavefront Δ can be obtained through a surface figure interferometer (Zygo-118). λ' is the wavelength of the light source

of the surface figure interferometer, and θ_m is the corresponding Littrow angle when the light source wavelength is λ'. Through Equation (8), the substrate error H and the line error W can be determined as follows:

$$\begin{cases} W = \dfrac{[\Delta(+1)-\Delta(-1)]d}{2m\lambda} \\ H = \dfrac{\Delta(+1)+\Delta(-1)}{4\cos\theta_m} \end{cases} . \tag{9}$$

Furthermore, the displacement measurement error L_{error} introduced by the grating surface figure can be solved through the wavefront information H and W corresponding to the two measurement beams, with the specific expression being:

$$L_{\text{error}} = [\Delta_1+\Delta_2]\frac{d}{2\lambda'} = \frac{1}{2\tan\theta_m}(H_1-H_2)+\frac{1}{2}(W_1+W_2) \quad . \tag{10}$$

Figure 10(a) (color online) shows the grating used in the experiment, while Figures 10(b) and 10(c) (color online) present the ±1st order diffracted wavefront results obtained using the Zygo interferometer. The red rectangular areas in the figures indicate the actual scanning regions of the detection spots in the experiment. By substituting the diffracted wavefront information into Equation (7), the line errors and substrate errors corresponding to the two detection spots scanning across the measurement line can be obtained, as shown in Figures 11(a) and 11(b) (color online). Further substitution into the formula reveals the impact of the combined effects of grating substrate error and line error on the displacement measurement results when the two measurement beams are non-coincident and incident on the grating. The error magnitude is around 6 nm, as depicted in Figure 11(c) (color online). Compared to the overall displacement deviation of 30 nm in Figure 8(a), this error accounts for approximately 20%. Under static conditions, the displacement noise of the grating interferometer is about 5 nm. During installation, the Abbe arm length between the laser interferometer measurement line and the grating interferometer measurement line is approximately 1 mm. Using an autocollimator (TA US 300-57, Trioptics) to measure the pitch and yaw angles of the corresponding linear displacement stage in this interval, the angles are found to be around 6 μrad in both directions, with the corresponding Abbe errors being approximately 6 nm each. The remaining error mainly originates from other environmental errors and electronic noise.

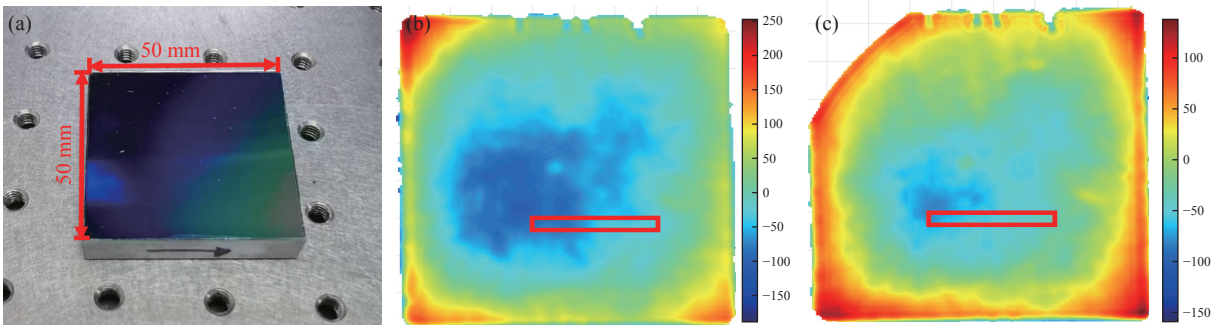

Fig. 10　(a) Scale grating. (b) Wavefront of +1st-order. (c) Wavefront of -1st-order

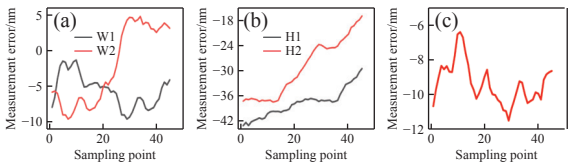

Fig. 11　(a) Line error. (b) Substrate error. (c) Grating surface error

4　Summary

This paper reported the design of a Littrow-type dual-axis homodyne grating interferometer based on a high-groove-density grating. Using an offset beam splitter prism in conjunction with right-

angled prisms and reflective mirrors, a simple and easily integrated dual-beam diffraction probe optical path—suitable for the simultaneous measurement of *xz* dual-axis displacement—was constructed. Experimental results show that after correcting for periodic nonlinear errors using the Heydemann algorithm, the short-term error is reduced to ±5 nm. The grating interferometer achieves a displacement resolution of 4 nm along the *x*-axis with a measurement error of ±30 nm within a 10 mm stroke; on the *z*-axis, it achieves a displacement resolution of 7 nm with a measurement error of ±100 nm within a 10 mm stroke. In future work, the design of the grating interferometer proposed in this paper will be iterated, with the interferometer mirror group being integrated and miniaturized, and the modeling and error analysis of a multi-probe multi-dimensional grating interferometer system will be completed.

References:

[1] LI M, CHEN T T, CHENG R, *et al*.. Dual-loop iterative learning control with application to an ultraprecision wafer stage[J]. *IEEE Transactions on Industrial Electronics*, 2022, 69(11): 11590-11599.

[2] LI X C, ZHU H Y, MA J, *et al*.. Data-driven multi-objective controller optimization for a magnetically-levitated nanopositioning system[J]. arXiv: 2007.02593, 2020.

[3] SCHMIDT R H M. Ultra-precision engineering in lithographic exposure equipment for the semiconductor industry[J]. *Philosophical Transactions of the Royal Society A: Mathematical, Physical and Engineering Sciences*, 2012, 370(1973): 3950-3972.

[4] CASTENMILLER T, VAN DE MAST F, DE KORT T, *et al*. . Towards ultimate optical lithography with NXT: 1950i dual stage immersion platform[C]. *Proceedings of the SPIE 7640, Optical Microlithography XXIII*, SPIE, 2010: 76401N.

[5] CIDDOR P E. Refractive index of air: new equations for the visible and near infrared[J]. *Applied Optics*, 1996, 35(9): 1566-1573.

[6] MA T CH, LI Z CH, CAO H L, *et al*.. A parallel denoising model for dual-mass MEMS gyroscope based on PE-ITD and SA-ELM[J]. *IEEE Access*, 2019, 7: 169979-169991.

[7] SHIBAZAKI Y, KOHNO H, HAMATANI M. An innovative platform for high-throughput high-accuracy lithography using a single wafer stage[C]. *Proceedings of the SPIE 7274, Optical Microlithography XXII*, SPIE, 2009: 72741I.

[8] TEIMEL A. Technology and applications of grating interferometers in high-precision measurement[J]. *Precision Engineering*, 1992, 14(3): 147-154.

[9] ZHOU W Y, SUN Y J, LIU ZH W, *et al*.. A random angle error interference eliminating method for grating interferometry measurement based on symmetry littrow structure[J]. *Laser & Photonics Reviews*, 2025, 19(11): 2401659.

[10] LI W H, WANG X Y, BAYANHESHIG, *et al*. . Controlling the wavefront aberration of a large-aperture and high-precision holographic diffraction grating[J]. *Light: Science & Applications*, 2025, 14(1): 112.

[11] BAI Y, HU P CH, LU Y F, *et al*.. A six-axis heterodyne interferometer system for the joule balance[J]. *IEEE Transactions on Instrumentation and Measurement*, 2017, 66(6): 1579-1585.

[12] ZHOU W Y, LI W H, LIU L, *et al*.. Bidirectional two-degree-of-freedom grating interferometer with biased Littrow configuration[J]. *Optics Communications*, 2024, 557: 130333.

[13] ZHU Y, ZHANG M, WANG L J, *et al*. . Two-degree-of-freedom heterodyne grating interferometry measurement system: US, 11307018B2[P]. 2022-04-19.

[14] ZHOU W Y, LIU ZH W, SUN Y J, *et al*.. Bidirectional Littrow double grating interferometry for quadruple optical interpolation[J]. *Optics & Laser Technology*, 2024, 175: 110751.

[15] ZHOU W Y, SUN Y J, LI W H, *et al*.. Polarization-folding ultra-wide spectral chromatic confocal line displacement sensor based on a binary lens[J]. *Optics & Laser Technology*, 2024, 177: 111152.

[16] HORI Y, GONDA S, BITOU Y, *et al*.. Periodic error evaluation system for linear encoders using a homodyne laser interferometer with 10 picometer uncertainty[J]. *Precision Engineering*, 2018, 51: 388-392.

[17] HSIEH H L, PAN S W. Development of a grating-based interferometer for six-degree-of-freedom displacement and

angle measurements[J]. *Optics Express*, 2015, 23(3): 2451-2465.

[18] GAO W, SAITO Y, MUTO H, *et al*.. A three-axis autocollimator for detection of angular error motions of a precision stage[J]. *CIRP Annals*, 2011, 60(1): 515-518.

[19] HSIEH H L, PAN S W. Three-degree-of-freedom displacement measurement using grating-based heterodyne interferometry[J]. *Applied Optics*, 2013, 52(27): 6840-6848.

[20] LI X H, SHIMIZU Y, ITO T, *et al*.. Measurement of six-degree-of-freedom planar motions by using a multiprobe surface encoder[J]. *Optical Engineering*, 2014, 53(12): 122405.

[21] LI X H, WANG H H, NI K, *et al*.. Two-probe optical encoder for absolute positioning of precision stages by using an improved scale grating[J]. *Optics Express*, 2016, 24(19): 21378-21391.

[22] SHI Y P, NI K, LI X H, *et al*.. Highly accurate, absolute optical encoder using a hybrid-positioning method[J]. *Optics Letters*, 2019, 44(21): 5258-5261.

[23] KIMURA A, HOSONO K, KIM WJ, *et al*.. A two-degree-of-freedom linear encoder with a mosaic scale grating[J]. *International Journal of Nanomanufacturing*, 2011, 7(1): 73-91.

[24] KIMURA A, GAO W, ARAI Y, *et al*.. Design and construction of a two-degree-of-freedom linear encoder for nanometric measurement of stage position and straightness[J]. *Precision Engineering*, 2010, 34(1): 145-155.

[25] KIMURA A, GAO W, ZENG L J. Position and out-of-straightness measurement of a precision linear air-bearing stage by using a two-degree-of-freedom linear encoder[J]. *Measurement Science and Technology*, 2010, 21(5): 054005.

[26] ZHU J H, WANG G CH, WANG S T, *et al*.. A reflective-type heterodyne grating interferometer for three-degree-of-freedom subnanometer measurement[J]. *IEEE Transactions on Instrumentation and Measurement*, 2022, 71: 7007509.

[27] LI S M, WANG J K, ZHANG W T, *et al*.. Real-time direction judgment system of sub-nanometer scale grating ruler[J]. *IEEE Access*, 2021, 9: 74939-74948.

[28] ZENG Q L, ZHAO ZH Y, DU H, *et al*.. Separation and compensation of nonlinear errors in sub-nanometer grating interferometers[J]. *Optics Express*, 2022, 30(26): 46259.

[29] SHIBAZAKI Y, KANAYA Y. Movable body drive method and movable body drive system, pattern formation method and apparatus, exposure method and apparatus, and device manufacturing method for continuous position measurement of moveable body before and after switching between sensor heads: US, 20120293788[P]. 2012-11-22.

[30] GUAN J, KÖCHERT P, WEICHERT C, *et al*.. A high performance one-dimensional homodyne encoder and the proof of principle of a novel two-dimensional homodyne encoder[J]. *Precision Engineering*, 2013, 37(4): 865-870.

[31] LV Q, WANG W, LIU ZH W, *et al*.. Grating based precision measurement system for five-dimensional measurement[J]. *Chinese optics*, 2020, 13(1): 189-202.

[32] LEE C K, WU C C, CHEN S J, *et al*.. Design and construction of linear laser encoders that possess high tolerance of mechanical runout[J]. *Applied Optics*, 2004, 43(31): 5754-5762.

[33] DE GROOT P J, BADAMI V G, LIESENER J. Concepts and geometries for the next generation of precision heterodyne optical encoders[C]. *Proceedings of the 31st Annual Meeting of the American Society for Precision Engineering*, ASPE, 2016: 146-149.

[34] 王磊杰, 郭子文, 叶伟楠, 等. 超精密空间分离式外差利特罗平面光栅编码器位移测量系统[J]. 光学 精密工程, 2022, 30(5): 499-509.
WANG L J, GUO Z W, YE W N, *et al*.. Ultra-precision spatial-separated heterodyne Littrow grid encoder displacement measurement system[J]. *Optics and Precision Engineering*, 2022, 30(5): 499-509. (in Chinese).

[35] LIN J, GUAN J, WEN F, *et al*. . Grating encoder for wide range three-axis displacement measurement[C]. *Proceedings of the SPIE 9446, 9th International Symposium on Precision Engineering Measurements and Instrumentation (ISPEMI)*, SPIE, 2014: 944602.

[36] LIN J, GUAN J, WEN F, *et al*.. High-resolution and wide range displacement measurement based on planar grating[J]. *Optics Communications*, 2017, 404: 132-138.

[37] 李晓天, 巴音贺希格, 齐向东, 等. 刻线误差与面型误差对平面光栅光谱性能影响的二维快速傅里叶变换分析方法[J]. 光学学报, 2012, 32(11): 1105001.
LI X T, BAYANHESHIG, QI X D, *et al*.. Two-dimensional fast fourier transform method of analyzing the influence of plane grating′s line error and surface error on grating′s spectral performance[J]. *Acta Optica Sinica*, 2012, 32(11): 1105001. (in Chinese).

[38] MAO X Y, ZENG L J. Design and fabrication of crossed gratings with multiple zero-reference marks for planar encoders[J]. *Measurement Science and Technology*, 2018, 29(2): 025204.

Author Biographies:

QIAN Xin-ge (2000—), male, born in Lishui city, Zhejiang Province, Master's degree candidate, obtained a bachelor's degree from Guizhou University in 2022, mainly engaged in research on grating interferometry measurement systems. E-mail: qianxinge22@mails.ucas.ac.cn

LIANG Xu (1993—), male, born in Changchun City, Jilin Province, Ph.D. holder, assistant research fellow, obtained a doctoral degree from the School of Precision Instrument and Optoelectronic Engineering at Tianjin University in 2022, mainly engaged in research on laser interference and grating precision displacement measurement. E-mail: liangxu@ciomp.ac.cn